

Hydrogel Microrobots Self-Assembled into Ordered Structures with Programmable Actuation

Jindrich Kropacek, Charlie Maslen, Bertjan van Dijk, Agustin Iniguez-Rabago, Johannes T.B. Overvelde, Alexandr Zubov, Jan Vrba, Petr Cigler, Frantisek Stepanek, and Ivan Rehor*

Sub-millimeter robots—microrobots—that can autonomously perform mechanical work at the microscale would radically change new areas of human activity such as micromanipulation, microfabrication, or healthcare. Sets of identical microrobots that can connect into different, larger structures open the possibility for a “universal” microrobotic unit that fulfills a large variety of functions derived from the structure that multiple units can be assembled into. The capability of individual hydrogel microcrawlers to self-assemble under confinement into periodically ordered planar structures is demonstrated. Subsequently, these can be bound together using light to form a solid porous sheet. The lateral shape of the sheet is imprinted during the binding process. Furthermore, the sheets bend into 3D structures, where the bending direction can be programmed. The resulting structures actuate anisotropically when exposed to heat or laser illumination and can be designed for various modes of operation, such as manipulation or untethered locomotion. The formation of ordered microstructures from individual mobile robots enables easier transport and remote assembly of these structures at the place of interest without the need for direct intervention.

1. Introduction

In the past decade, numerous microscopic (i.e., below 1 mm) objects, capable of active, untethered locomotion—microrobots—have been reported. These systems include magnetic and electric field-driven nano/microparticles, active colloids moving by dielectrophoresis, bubble-driven micro-objects, and reactive microswimmers.^[1] Another important class of microrobots locomotes through forces generated during mechanical actuation cycles, similar to conventional macroscopic robots. The locomotion provided by mechanical actuation provides robust and variable motility at the microscale (jumping,^[2] crawling/walking,^[3–8] swimming)^[9–11] in both wet and dry environments and can also be used for other applications such as manipulation of other objects.^[12–14]

To simplify the design of such microrobots, they are often constructed from soft, responsive materials which actuate through deformations. Due to the size of the robot, the energy source is rarely integrated into the robot body and is delivered from the environment.^[1] Examples include chemical propulsion,^[5] magnetic field,^[9,12,14] or light.^[15–17] Several principles for light-driven locomotion have been demonstrated, including liquid crystal elastomers which respond to illumination by internal phase transitions resulting in shape changes,^[1,3,4,10] or thermoresponsive hydrogels, loaded with highly absorptive species.^[18–20]


Importantly, the actuation observed in these robots is often an interplay between stimuli and their shape. As a result of their fixed design, existing microrobots are typically specialized for a specific task such as locomotion, rotation, or manipulation, such that a new task requires the development of a new dedicated robot. For example, a microrobot that can navigate to hard-to-reach places will look very different from a microrobot that is optimal at performing manipulation tasks, yet both functions might need to be combined. Here, modular robots hold promise to overcome such specialization, being built from connectable subunits, that can be rearranged to adapt to multiple tasks.^[21–23] However, the assembly and organization of the individual robots remain a complex challenge across all length scales.

Macroscopic robot units typically organize themselves based on the internal programming of each elemental unit.^[24] Such

J. Kropacek, C. Maslen, B. van Dijk, A. Zubov, J. Vrba, F. Stepanek, I. Rehor
Faculty of Chemical, Engineering
University of Chemistry and Technology Prague
Technicka 5, 166 28, Prague 6 Prague, Czech Republic
E-mail: rehor@vscht.cz

A. Iniguez-Rabago, J. T. B. Overvelde
Soft Robotic Matter Group
AMOLF
Science Park 104, 1098 XG Amsterdam, Netherlands

P. Cigler, I. Rehor
Synthetic Nanochemistry Research Group
Institute of Organic Chemistry and Biochemistry of the Czech Academy of Sciences
Flemingovo nam. 2, 160 00 Prague, Czech Republic

 The ORCID identification number(s) for the author(s) of this article can be found under <https://doi.org/10.1002/aisy.202300096>.

© 2023 The Authors. Advanced Intelligent Systems published by Wiley-VCH GmbH. This is an open access article under the terms of the Creative Commons Attribution License, which permits use, distribution and reproduction in any medium, provided the original work is properly cited.

DOI: 10.1002/aisy.202300096

onboard controlling systems are not compatible with microscale robots; hence, these are typically operated and organized externally. Magnetic fields can be used for both robot positioning and connection, but does not allow the independent addressing of individual robotic units—the field affects the behavior of all microrobots within it. This can be partially overcome by collections of heterogeneous microrobots with different responses to the magnetic field^[25] or a combination of an active unit with passive ones.^[26] Such strategies, nevertheless, result in relatively small ensembles comprising only several units. A similar bottleneck—limited ability to address individual units independently—is coupled to passive unit organization by fluidic^[27–29] or electrophoretic^[30] forces.

The dimensions of microrobots make them suitable candidates for autonomous self-organization *via* self-assembly, that is, iterative spontaneous minimization of the system free energy. The arrangement of the self-assembled structure is defined by the properties of the units such as their shape,^[31–34] and material anisotropy,^[35] as well as properties of the entire system, for example, experimental area size and shape, temperature, or presence of electromagnetic fields.^[34,36] Tailoring these variables to achieve the desired structure may be viewed as a viable alternative to *in silico* programming of macroscopic swarming robots,^[33,37–41] or active self-organization of mobile microrobots.^[42] Note that microrobots are typically too large to exhibit Brownian motion ($>2\ \mu\text{m}$) and so cannot explore their phase space to overcome local maxima at their free-energy hyperplane.^[43] Still, simple ordered structures can be assembled at these lengthscales,^[43–48] which may be useful for microrobotics applications. Self-assembly at these lengthscales is typically restricted to two spatial dimensions, due to the positive buoyant mass of the building blocks in the media and their rapid sedimentation. Subsequent folding of 2D (self)assembled structures may overcome the limitations of the 2D assembly and greatly expand their application potential.^[24] Yet the main drawback of the self-assembly approaches lies, again, in an inability to address the individual building blocks independently. Hence, the strengths and drawbacks of described methods of individual

manipulation and organization strategies indicate that the optimum, between individually addressable building blocks and their scalable parallel organization, would likely require a combination of more strategies.

In this work, we demonstrate that serially manipulated microrobots can be first directed and then allowed to self-assemble into ordered periodic structures. We use microrobots that are composed of a hydrogel, which allows us to utilize the chemical properties of the microrobots to subsequently bind multiple microrobots covalently into a single structure. Furthermore, owing to the diffusion of solutions through the hydrogels, this method of chemical binding enables us to program specific off-plane deformation into the resulting structure. A gradient in the binding chemical reaction rate along the structure height emerges spontaneously and is responsible for controllable out-of-plane deformation (buckling) of the structure, referred to as so-called pop-up deformation. This gradient is further responsible for the structure's anisotropic actuation, enabling its use as a milliscopic crawler or grabber.

2. Results and Discussion

2.1. Building Blocks

Previously, we introduced microscale hydrogel crawling robots (crawlers) that actively move in an aqueous environment via light-induced reciprocal shrinking and expansion cycles.^[20] The crawlers are actuated photothermally since they consist of thermoresponsive polymer poly(*N*-isopropylacrylamide) (PNIPAM) with entrapped plasmonic nanoparticles that absorb focused light. The hydrogel is heated by the absorbed energy, which results in its reversible isotropic shrinkage. Pulsed irradiation with a focused beam results in cyclic shrinkage and expansion of the irradiated section of the crawler (Figure 1A). During each cycle, a $100\ \mu\text{m}$ -diameter disc-shaped crawler moves in the direction away from the beam by $\approx 5\ \mu\text{m}$. We previously explained this displacement by friction hysteresis

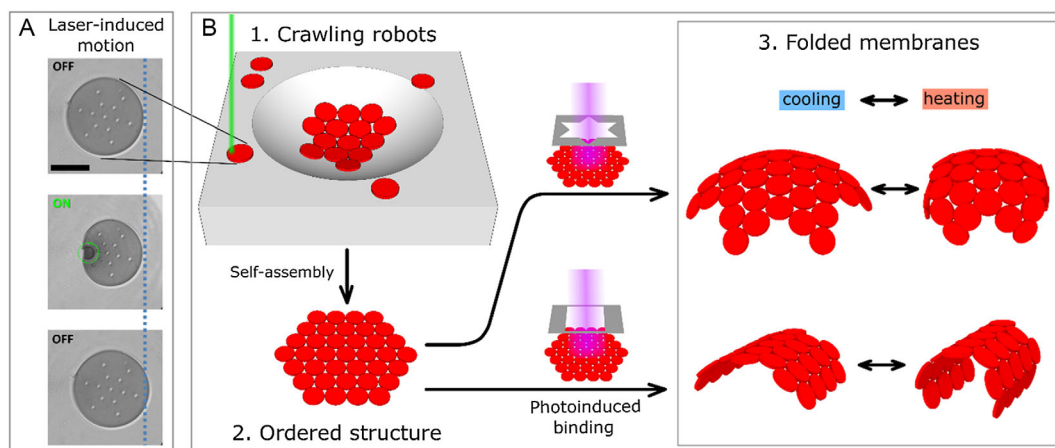


Figure 1. Self-assembly of disc-shaped crawling robots into actuating structures. A) The disc crawls when irradiated with focused beam pulses, in the direction away from the beam (beam area indicated in green, scale bar = $50\ \mu\text{m}$). B) Schematics of the entire process: 1) Crawlers are actively navigated to reach the depression, after which they passively self-assemble. 2) Assembled crawlers are bound in a sheet *via* photoinduced covalent crosslinking; 3) The sheet deforms (buckles) and actuates by closing/opening when exposed to heat cycles or laser illumination.

between the contraction phase and the expansion phase and constructed a predictive model describing the crawling process.^[20] The direction of each crawler step is set independently by the irradiation point as the crawling always follows the vector from the irradiation spot to the crawler center.

Connecting several individual microrobots together in a defined manner may extend their functionalities beyond mere crawling locomotion; however, such a process is limited to several microrobots, due to its serial nature.^[49] Complex, organized, actuating structures require at least tens of elemental microrobot units and, hence, are not accessible by such top-down directed assembly methods with acceptable throughput. Therefore, we adopted a new approach to robotic units' organization—self-assembly (Figure 1B). As in our previous work,^[49] we elected to use disc-shaped crawlers as this shape allows full freedom to translate in any direction away from the irradiation spot. Furthermore, the self-assembly of discs enables the formation of densely packed, hexagonal assemblies.

2.2. Crawler Assembly

We consider that in a real-life application, the crawlers would typically crawl in an uneven environment (they can crawl up to 20° incline)^[20] and decided to exploit the opportunities of such terrain topography to induce robot–robot interactions and assembly. We constructed a model environment for the robot self-assembly—a flat surface with a depression (Figure 2A). Disc-shaped crawlers were deposited onto the flat region surrounding the depression. They were then navigated one by one to the edge of the depression. To facilitate the process, an automated computer-driven platform was used to manipulate the crawlers to specific areas.^[49] Once a crawler crosses the edge of the depression, it begins to slide down the slope toward its center. The sliding is purely passive, induced by gravity, and does not require actuation (more on sliding platelet microgels in ref. [48]). The potential energy of each disc in the depression is defined by

its elevation, dictated by its distance from the depression center. For a system comprising multiple discs, the total potential energy equals the sum of the potential energies of individual discs (being constrained by contact); hence, the more densely the discs are packed around the well center, the lower the potential energy of the system. Although the discs do not exhibit any random motion (thermal or agitation) and, hence, cannot explore their phase space,^[48] we observed the ordering of the discs into the minimum potential energy state—hexagonal packing—at the bottom of the depression. The crawling and assembly of the first 10 discs and the final assembly after 24 discs crawled into the well and assembled is depicted in Figure 2A,B, respectively, and Video S1, Supporting Information.

Knowing that crawling discs self-assemble at the bottom of the depression into a hexagonal packing, we decided to study the self-assembly process in greater detail. We conducted a series of experiments, where we avoided the time-consuming crawling into the well. Instead, a dispersion containing ≈ 300 discs was pipetted directly into a round-bottom well to sediment and assemble in parallel. Moreover, this experimental arrangement simulated other possible ways of disc delivery to the place of interest, such as by a fluid flow.^[27,50] The discs, settled on an inclined plane, slide toward the well center and form densely packed assemblies, structurally similar to those observed in the case of active crawling into the depression (Figure 2C, Video S2, Supporting Information). The parallel assembly process took several hours after which no further rearrangements in the structure were observed. The process typically resulted in a single hexagonal crystal or several crystal domains (2–3) separated by line defects (examples of assemblies can be found in Figure 3, 4 and 5). One missing disc in the regular assembly—a vacancy—is a typical point defect in the assembly. Vacancies can be removed from the lattice, using active crawling of the discs—the adjacent discs are simply crawled to the appropriate positions (detailed description can be found in Section S1, Figure S1, and Video S3, Supporting Information).

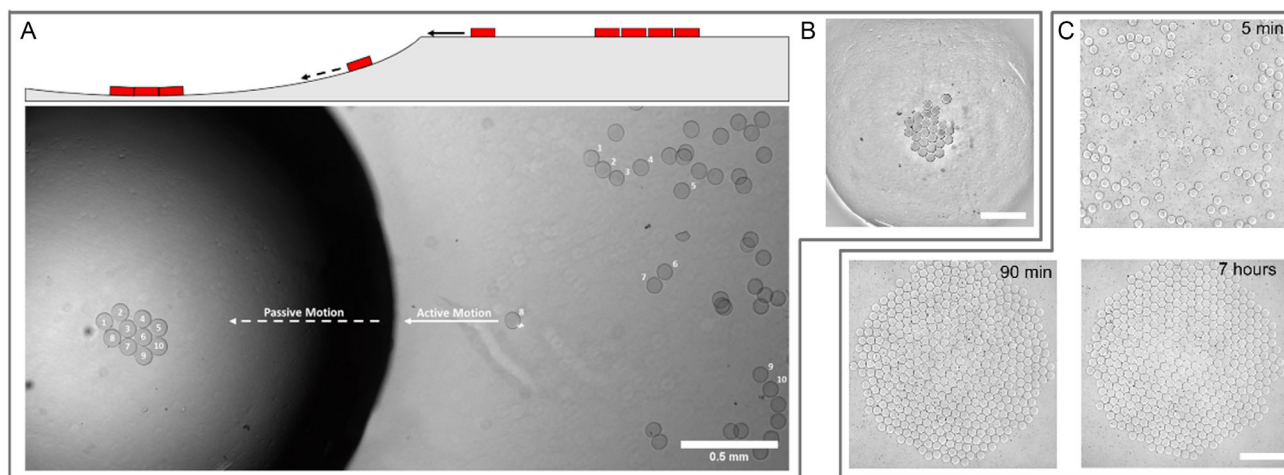


Figure 2. Serial and parallel self-assembly. A) Disc-shaped microrobots crawl to the edge of the depression and consecutively passively slide to its center, where they form a densely packed hexagonal assembly. The process is shown for the first ten discs as a montage from multiple micrographs displaying the individual stages of the process. B) Discs passively sedimented at the bottom of depression after crossing its edge by active manipulation and C) assembly of discs 5, 90 min, and 7 h after addition. After this time, the positions of the mutual discs remain unchanged (all scalebars = 0.5 mm).

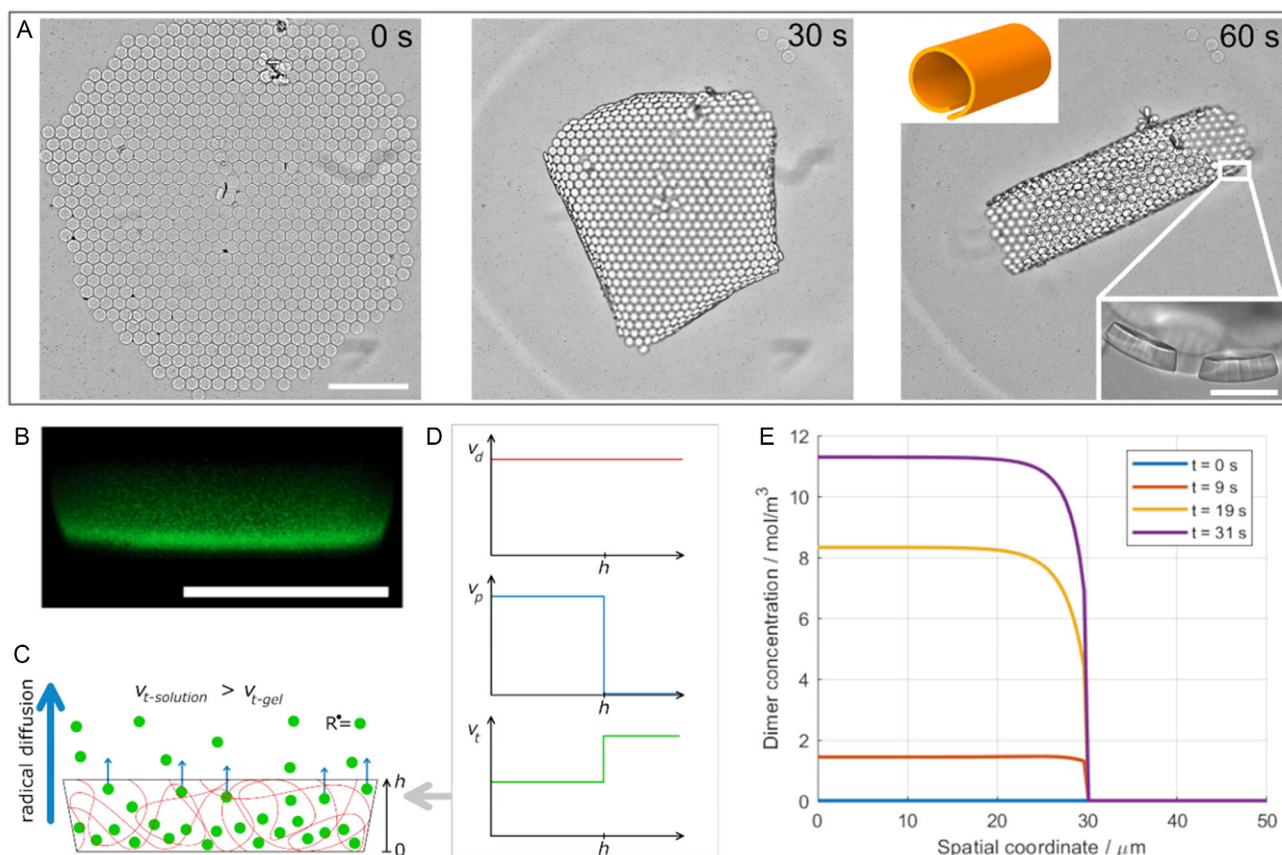


Figure 3. Disc binding into a folded sheet. A) Binding of assembled discs. Upon UV illumination, the assembled discs are bound to form a single sheet, which buckles with its outer rim bending downwards (scale bar = 0.5 mm). Due to the mechanical strain, the sheet forms a roll (indicated in the upper left inset). Right corner inset: detail of connected discs from the side showing their deformation from the original cylindrical shape (scale bar = 50 μm). B–E) Crosslinking density gradient along the particle height. B) Sideview of a disc obtained with scanning confocal microscopy. Methacrylated fluorescent dye was added to the binding solution to monitor the relative rates of the radical crosslinking at various heights of the disc. The bottom side of the disc is brighter than the top one, indicating a higher number of crosslinking events in that section (scale bar = 50 μm). C) The difference in the termination rate inside and above the microgel results in a diffusive flow of the radicals from the top sections of the gel to the solution, which results in a gradient in its crosslinking density. D) Schematic spatial profiles of individual reaction rates along the vertical coordinate h (from microgel bottom up to the solution) at the start of the binding—initiation (v_d), propagation (v_p), and termination/recombination (v_t). E) Temporal evolution of crosslinks (i.e., terminated dimers) in the microgel and aqueous solution above, as predicted by the mathematical model. The microgel phase is assumed for spatial coordinate $z = (0, 30 \mu\text{m})$, while the aqueous phase lies at $z = (30, 100 \mu\text{m})$. A detailed description of the developed model is provided in Section S6, Supporting Information.

The discs exhibit a strong tendency to arrange into dense hexagonal packing under various geometries. We tested spherical depressions, ranging in diameters ranging from 0.5 to 2 cm (Figure S2A, Supporting Information), yielding similar assemblies to those in Figure 2C. Additionally, packing occurred also at much lower inclines. Even a small tilt of the surface ($\approx 2^\circ$) cause the discs to slide since there is no static friction (as we described previously)^[48] and, once set in motion, these arrange into the packing. Hence, densely packed structures could be obtained on flat inclined plane under tilts between $\approx 2^\circ$ and 10° (Figure S2B,C, Supporting Information) (higher tilt angles lead to structure collapse and formation of multiple layers). We discuss the microgel packing on the inclined plane in detail elsewhere.^[48] Furthermore, we observed clusters of packed discs on almost flat surfaces with height differences between the lowest and the highest point of the assembly around 20 μm (Figure S2C, Supporting Information).

2.3. Binding and Buckling

As a next step, we bind the assembled discs by photoinduced crosslinking of remnant acrylate moieties present in the hydrogel. A similar methodology has been previously used for the binding of acrylate microgels by others,^[51] as well as by our group.^[48] During the binding process, the discs bind into a single sheet while their diameter reduces by $\approx 16\%$ (Figure 3A, Figure S3, Supporting Information). The disc shrinkage is expected—as the acrylates in the gel are coupled together, new crosslinks are created within the hydrogel, and its crosslinking density increases. As the equilibrium volume of a hydrogel is given by the equilibrium between the osmotic swelling and macromolecular chain strain, the increase of the crosslinking density leads to shrinkage of the gel disc during the binding.^[52]

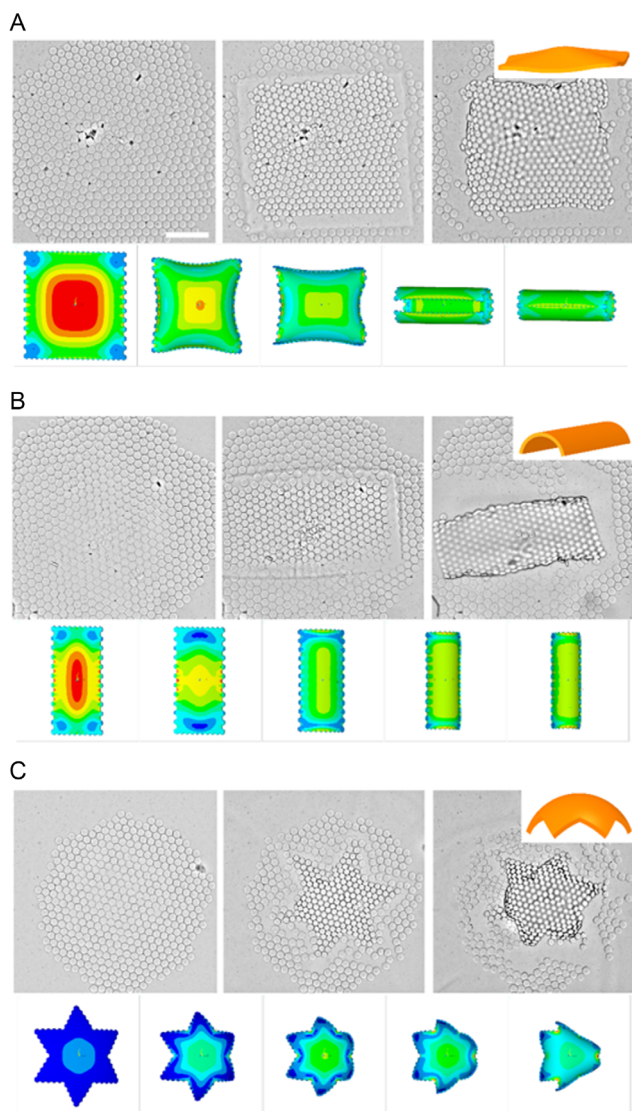


Figure 4. Bending of various lateral shapes defined by the illuminated area. A) square, B) rectangle, and C) star (scale bar = 500 μm). The deformations received from the simulations (with increasing Von Mises stresses indicated in the color scale from blue to red) show identical behavior at the initial stages with all three shapes. With star and square, the greater degree of deformation in finite element simulations, compared to experiments, resulted in the breaking of the symmetry, not paralleled in the experiments.

At the beginning of the binding process, the assembly lies flat at the bottom of the depression, while as the binding reaction progresses, it begins to deform, its outer rim bending downwards (Video S4 and Figure S4, Supporting Information). The sheet deformation continues after the illumination source is turned off for another 10–20 s. Since the disc diameter does not change during this ‘dark’ phase, we argue that the delay in the buckling originates from the slow relaxation of the mechanical stress in the sheet, caused by friction and viscous forces acting against the light-induced sheet morphology changes (discussed later in greater detail). Small assemblies

(comprising ≈ 50 –100 discs) create dome-shaped structures (Figure S4, Supporting Information), while the large ones (comprising ≈ 300 –500 discs) typically lose the radial symmetry and form a roll as the one seen in Figure 3A. The sheet buckling originates from the deformation of the individual discs as their bottom side shrinks more than their top side (Figure 3A inset, and Section S2, Supporting Information). Since the individual discs are connected by their sidewalls during the binding process, the deformation is transferred to the entire sheet. Buckling has previously been well described experimentally and theoretically in numerous publications with bilayers—sheets composed of two layers, each undergoing independent volumetric change.^[53–56] In our case, the discs are composed of a single material and the strain is induced by their anisotropic shrinkage (in the out-of-plane direction) during the binding.

2.4. Molecular Mechanism of Buckling

The following section describes the mechanism of sheet buckling, originating from different rates of polymerization along the disc height during their binding. We provide a detailed description of the phenomenon and the experiments we conducted to identify it in the Section S3, Supporting Information. Here, for the sake of brevity, we merely summarize our main findings.

The binding is provided by photoinduced radical polymerization, comprising multiple chemical reactions that can be divided into four stages. First initiator decomposition where a photoinitiator molecule cleaves to form a primary radical due to the absorption of a photon. The rate of the primary radical formation is proportional to the photoinitiator concentration and the light intensity. The absorbance of the photoinitiator solution in the studied system is negligible over the height of the hydrogel disc (justification in Section S4, Supporting Information) and, thus, the production rates of the primary radicals (ν_D) inside and just above the hydrogel are almost identical (Figure 3D). In the second stage—initiation—some of the radicals created inside the hydrogel react with the remnant acrylate groups, creating monomer radicals. In the third stage—propagation—these monomer radicals react with nearby monomers to form new crosslinks inside the hydrogel—dimer radicals—and potentially grow further. In the fourth stage—termination—any two radical species created in the system collide in the solution and recombine. Obviously, upon continuous illumination in the discussed system, all the reaction steps occur simultaneously, their rates being governed by their rate constants and the immediate concentration of the reactants. The recombination (termination) rate constant of the radicals is proportional to their collision frequency, which depends on their mobility, that is, the radical diffusion coefficient D_R in the medium.^[57] Note that all radical species containing monomers are immobilized in the network and only the primary radicals can freely diffuse. The diffusion coefficient of a small molecule such as the primary radical is lower inside the hydrogel than in the aqueous medium above the hydrogel (estimation in the Section S5, Supporting Information). Hence, the recombination of radicals proceeds faster in the solution than inside the gel in an analogy to the well-known gel effect (also known as the Trommsdorff effect

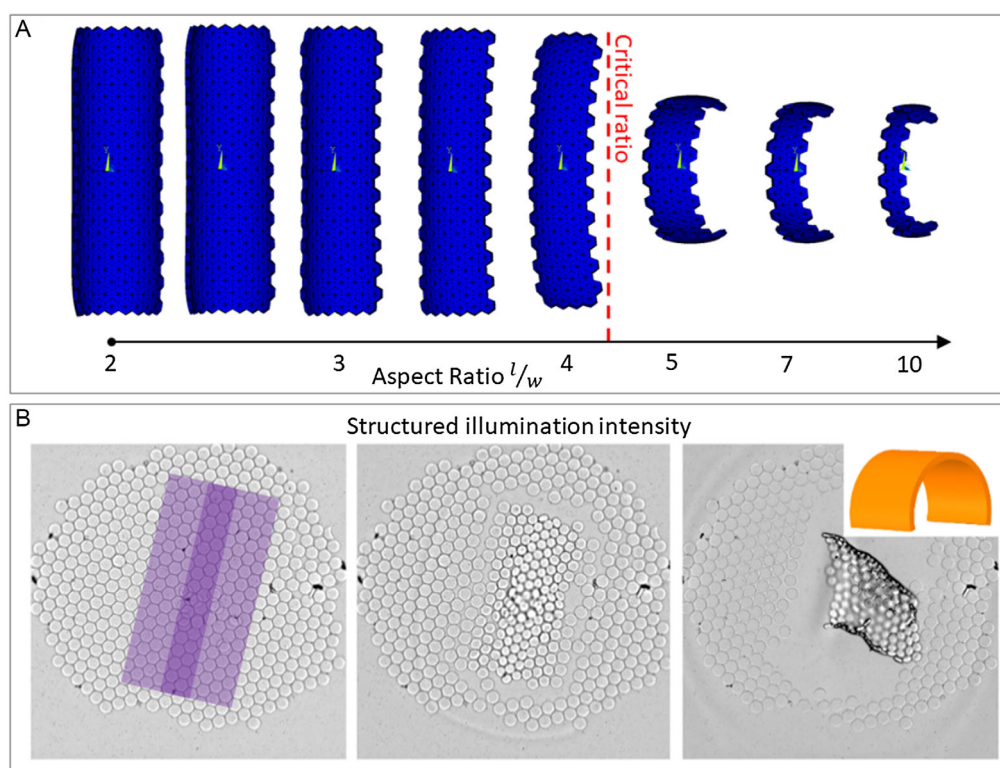


Figure 5. Programming of rolling direction. A) High-aspect-ratio rectangles (aspect ratio length/width, $l/w > 5$) roll along the short side, while lower-aspect-ratio rectangles roll along the long side. B) Low-aspect ratio rectangle (2) can be rolled along the short side, using a mask with a fully transparent high-aspect-ratio central stripe and semitransparent sides (indicated in purple). The discs in the central stripe buckle faster and dictate the rolling direction of the entire sheet. Uniform illumination of the same aspect ratio results in the opposite rolling direction (Figure 4B).

or Norrish–Smith effect) described for free-radical polymerization.^[57] Inevitably, the difference in these recombination rates over the course of the illumination results in a lower concentration of primary radicals (R_1) outside the gel compared to the inside (shown schematically in Figure 3C). Consequently, a fraction of the radicals from the upper section of the gel diffuses from the gel to the solution, creating a gradient in the primary radical concentration along the gel height. This gradient will be reflected in variable initiation, and propagation rates along the hydrogel height and, ultimately, in a gradient in the crosslinking density, which we confirmed experimentally (Figure 3B) as well as by finite volume model (Figure 3E). As the equilibrium volume of a hydrogel is given by the equilibrium between the osmotic swelling and macromolecular chain strain, the local increase of the crosslinking density leads to local shrinkage of the gel disc.^[52] A detailed description of the experiments identifying the phenomenon as well as the finite volume model can be found in Section S3–S7, Supporting Information.

2.5. Folding Behavior

The buckling of the sheets is induced by the mechanical stress generated during the anisotropic shrinking of each disc. The preferred biaxial shrinkage, expressed on the level of individual discs, is transferred to the entire sheet. With small sheet lateral dimensions, the stress can be tolerated, the sheets do not reach the critical

buckling transition, and dome-shaped structures are obtained (Figure S4, Supporting Information). Occasionally the stress accumulated in the bending structure is too large and the sheet cracks along the disc–disc binding spots to release it partially.

For larger sheets comprising several hundred discs, for which the lateral dimensions exceed the thickness by almost two orders of magnitude, the mechanical stress buildup in the material eventually results in unidirectional buckling. The lowest energy sheet conformation corresponds to a roll, as has been previously described theoretically^[56,58] and observed experimentally with bilayers^[53,55] and gel sheets with a gradient in crosslinking density along their height.^[59] Indeed, for larger assemblies we observe a loss of radial symmetry in the buckling structure and the formation of a roll (Figure 3A). The roll diameter varies somewhat between the individual experiments and is likely given by the assembly size and the number of defects (dislocations, point defects, discs in the second layer). Occasionally, the structure freezes in an intermediate state with threefold symmetry (Figure S5, and Video S5, Supporting Information). We have not observed any impact of the hexagonal disc ordering on the rolling direction; hence, we assume it has negligible effect and the plate is mechanically isotropic.

Given the similarity of the behavior of these sheets to the folding behavior observed in bilayer sheets, we believe that the lateral shape of the sheets can be designed to generate specific programmed folding behavior. To test this, we create sheets of

various shapes in the lateral plane by restricting the irradiated area, since only the discs directly exposed to the light are connected. As expected, we observed that the sheet's lateral shape is driving the buckling process (Figure 4). Illumination of a square area does not result in a roll and the sheet is deformed just by rolling the middle sections of the edges underneath with corners spiking out of the structure (Figure 4A and Video S6, Supporting Information). Rectangular membranes roll preferably along the long side (Figure 4B and Video S7, Supporting Information). With the star-shaped mask, the presence of the 'incuts' in the design between the star points reduce the central continuous area, enabling biaxial bending (Figure 4C and Video S8, Supporting Information), analogous to that observed with small assemblies, as described above.

To gain an understanding of the underlying principles that govern the folding in our system, and to be able to qualitatively predict the folding behavior of the sheets, we developed a numerical finite-element model in the commercial software package Ansys. For simplicity, we assume that the anisotropic swelling behavior can be captured by modeling a bilayer sheet, for which we apply different swelling ratios between both layers. We performed dynamic simulations where we increased the magnitude of the swelling in the first part of the simulation and allowed it to relax in the second part. Moreover, to reduce computational cost (increase mesh size), we decided to perform all simulations on assemblies of hexagons, since they provided almost identical data to the hexagonally assembled discs (Justification in Section S7, Supporting Information).

Before determining the folding behavior of various disc assemblies, we first investigate the effect that damping has on the folding behavior observed in the simulations. The damping in real samples is realized by the viscous drag of the aqueous medium as well as friction exerted on those parts of the folding structure that are in direct contact with the substrate. The friction force exerted on hydrogel discs is linearly proportional to the shear velocity.^[20,48] Thus, both viscous and friction drag scale in the same manner in the system, which justify the use of a single damping constant in the model. While it is difficult to exactly determine the interaction of the sheet with the environment and the damping behavior, our model can, at least qualitatively, predict how friction and viscous drag can influence the folding behavior of the disc assemblies. To achieve this, we simulate the folding behavior of a rectangular sheet with lateral dimensions aspect ratio 2:1 and vary the viscous damping behavior (Figure S6, Supporting Information). Interestingly, we find that the sheets show preferential rolling along the long or short side, depending on the damping constant. At low damping, we find that the sheets first roll along the long side and then they relax to roll along the short side. At high damping, we see that the sheet does not have enough time to relax to the short-side roll and always rolls preferentially around the long side. In experiments, the binding of identical rectangular sheets provided structures rolled along the long side, that is, corresponding to the high-damping scenario (Figure 4B). The presence of significant damping in the system is also supported by the observed slow dynamics of the rolling. The structure relaxes to its equilibrium folded state gradually and typically after the light source had been already turned off for more than 10 s, no further binding reactions occur (Video S4, Supporting Information).

We next use this model to simulate the square, rectangle, and star sheet deformation (Figure 4) and trace their mean and Gaussian curvature for increasing values of the stimulus. The deformations obtained from simulations fit qualitatively to those in the real samples. The biggest difference is the greater deformation of the sheets in the simulations. The deformation in the simulations was set from the microscopic observation of the deformed discs (such as in the inset in Figure 3A). This quantitative difference is responsible for qualitatively different equilibrium deformations in the square and the star. Both these sheets initially deform identically in the simulation and experiments. The greater deformation in the simulation is responsible for the deviation of the simulation from the experiment in the latter stages of the process—the fourfold symmetry in the square breaks and the sheet rolls, the sixfold symmetry in the star also breaks to the threefold. This discrepancy could be ascribed to the complexity of the chemical binding process: the sheet deformation is delayed after the binding reaction; hence, one may expect that the top edges of the discs would be bound the firmest, while the bottom edges (adjacent to the well bottom) would be less so, since these are retracted from each other because of disc shrinking. Hence, the disc deformation of the individual discs is not completely transferred to the deformation of the entire sheet. Nevertheless, the qualitative behavior of the sheets in the simulations matches the experiments and they allow us to predict the bending behavior, which we use in the next section for programming the bending direction.

2.6. Deformation Programming

Here, we change the rolling direction of rectangular sheets of aspect ratio 2:1 by spatially modulating the illumination intensity and, hence, the timing of the bending at various parts of the sheet (Figure 5 and Video S9, Supporting Information). Instead of an entirely transparent mask, we used a mask with a fully transparent, narrow stripe in the center oriented parallel to the long edge of the rectangle and surrounded by segments with reduced transparency. Upon illumination through this mask, the crosslinking reaction proceeds faster in the central narrow section. Hence, the discs in this section deform sooner than those in the rest of the illuminated area. Our simulations revealed that for high-aspect-ratio rectangles, rolling along the short side is preferred (Figure 5A). Since the aspect ratio of the central section is 8:1, the strip will start rolling along the short side, dragging loosely connected discs from the lower-intensity illuminated area, before these significantly shrink and deform. In other words, one could think of the central stripe as a template that drives the whole structure to the short-side bent conformation.

A similar effect of preferential rolling with the patterned mask can be achieved by subsequent illumination of distinct sections of the assembly. First, the illumination of a thin stripe along the assembly for 5 s, followed by global illumination, allows for controlled directional rolling of the assemblies always in the direction of the stripe (Section S8 and Video S10, Supporting Information).

2.7. Thermal Actuation

Prepared assemblies are thermoresponsive, composed of PNIPAM discs. Thus, they undergo a volumetric change when

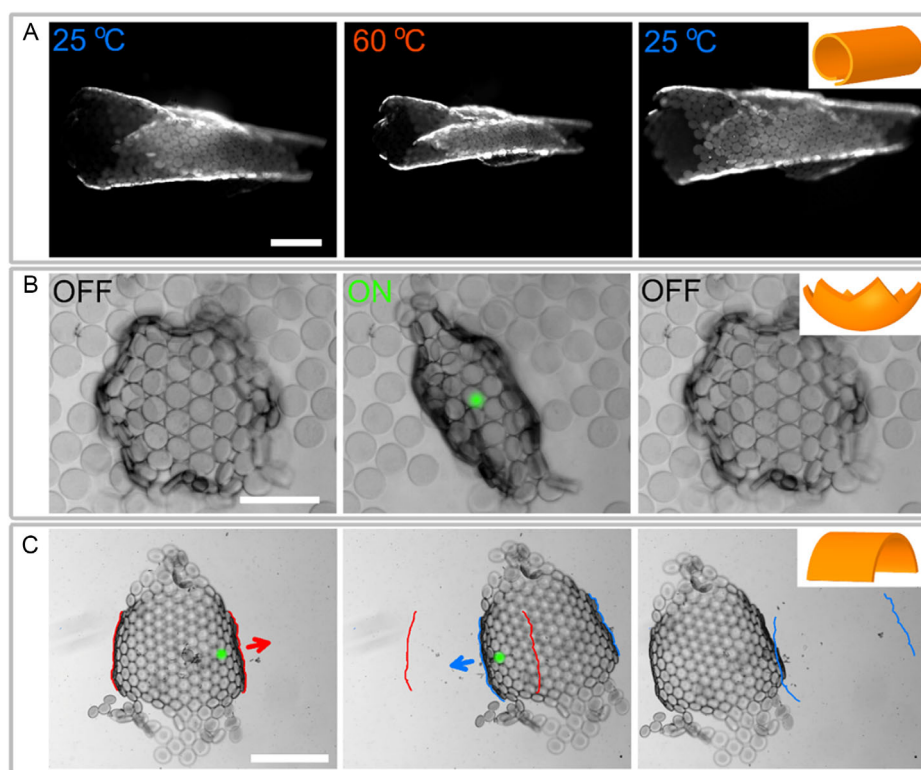


Figure 6. Actuation upon global heating or local laser illumination. A) When heated, the tube contracts, decreasing its diameter (scale bar = 0.5 mm). B) Aiming laser at the center of the starfish induces its contraction in a grabbing fashion (scale bar = 0.25 mm). C) A bent ribbon can be crawled when irradiated by laser pulses. The position of the laser determines the crawling direction. The positions of the front and rear edges in contact with the substrate are indicated in red (motion to the right, distance traveled in 40 steps) and in blue (subsequent motion to the left, distance traveled in 44 consecutive steps) (scale bar = 0.5 mm).

exposed to elevated temperatures. The relative shrinkage of the heated PNIPAM gel depends on its local crosslinking density.^[60] Thus, exposing the assemblies to elevated temperatures changes the curvature of a rolled sheet (Figure 6A and Video S11, Supporting Information) or induces a grabbing-like motion in a buckled star-shaped assembly (Figure S7 and Video S12, Supporting Information). It is also possible to induce the actuation of the buckled sheets by local laser heating. A star-shaped microgripper closes when illuminated with a laser at its center (Figure 6B and Video S13, Supporting Information), where the open–close cycle is induced by laser pulses with a frequency around 0.5 Hz (contraction ≈ 0.5 s, expansion ≈ 1.5 s). Notably, similar star-shaped gripper structures have been previously fabricated from bilayered materials.^[14,61] Another example is a folded sheet, analogous to the one in Figure 5, which was exposed to pulsed laser illumination to change its radius of curvature cyclically (Figure 6C and Video S14, Supporting Information). Aiming the laser closer to one edge of the sheet in contact with the substrate causes the sheet to displace with every actuation cycle in the direction toward the beam by $\approx 15 \mu\text{m}$ (Figure S8, Supporting Information). In this fashion we were able to consistently locomote the sheet hundreds of micrometers in both directions, choosing the direction simply by the illumination spot. We expect directional locomotion is caused by some underlying phenomenon that breaks the

reciprocity of the seemingly 1 degree of freedom (DOF) motion. Such phenomena may have complex causes such as nonuniform heat transfer through the structure, causing small differences between the collapse–re-expansion pathway, or differences in local friction at contact points, given by different contact angles (a phenomenon utilized previously for a 1 DOF motion).^[62,63] We are currently investigating this crawling mechanism in greater detail, the currently presented data just serves as an illustration of the opportunities the reported system provides. As an example of practical application of such assembled sheets, we used it to transport a 0.4 mm-large glass sphere (Figure S9, Supporting Information). The buoyant mass of the sphere is roughly 30 times higher, than that of the assembly, though we are able to achieve some displacement. The buoyant mass difference of such sphere with respect to one disc is almost 4 orders of magnitude, making the manipulation impossible. The experiment shows, that it is possible to increase the size and weight of the manipulated object using multiple connected robots for the manipulation.

3. Conclusion

In this work, we show a modular microrobotic system relying on self-assembly. We fabricated elemental robotic units, capable of

untethered locomotion over a substrate. Self-assembly of these microrobots directly on the substrate orders them into milliscopic, densely packed, 2D structures. These are subsequently bound into porous sheets. During this binding, an off-plane deformation of the entire sheet occurs. We qualitatively described the molecular processes responsible for this deformation and created a predictive model of the deformation, allowing for in silico design of the desired membrane shapes. Owing to the deformation, the sheets are capable of anisotropic actuation performing simple tasks, such as grabbing motion or crawling. In this entire process of milliscopic robot formation, the disc fabrication is the only step that requires specific microfabrication techniques—all the other steps proceed directly on a substrate at the place of interest and are triggered remotely by light. The on-the-spot construction of the final robot from the elemental units enables rapid prototyping of microscale actuating structures directly at the place of interest even in constrained or problematically accessible areas, as long as these are accessible optically. Furthermore, the ability to control the resulting 3D shape of the final robot by, in effect, controlling the rates of chemical reactions within the internal structure of the constituent microrobots after their production exploits hydrogel perfusion—a unique property among materials for microrobotic systems. We demonstrate that the use of chemical approaches, namely, self-assembly and chemical binding, in microrobotics not only represents a practical alternative to complicated directed assembly and subsequent magnetic or interlocking mechanisms, typically used at the macroscale, but also surpasses the previously reported modular microrobotic systems. The combination of individually addressable light-fueled robots with parallel self-assembly process enables manipulation with large microrobot collections, while keeping the ability to move individuals within the assembly. To our best knowledge, this has not been achieved with magnetic forces, propelled swimmers, nor other distinct branch of current microrobot control mechanisms.

A future combination of here-described processes with reversible binding of the units, for example, via coulombic or host–guest molecular interactions, that has been previously shown to effectively bind gel objects together will provide reconfigurable, modular milliscopic actuators. Such systems may find application in various fields including implantology and microsurgery, soft actuation, or metamaterials construction.

4. Experimental Section

Materials: *N*-isopropylacrylamide (NIPAM), poly(ethylene glycol) diacrylate (PEGDA, average $M_n = 700$ Da), trisodium citrate, fluorescein-*O*-methacrylate, Tween 20, and Pluronic F127 were purchased from Sigma Aldrich. Tetrachloroaurate trihydrate ($\text{HauCl}_4 \cdot 3\text{H}_2\text{O}$) was purchased from Alfa Aesar. SYLGARD 184 silicone elastomer kit (elastomer base + curing agent), used for the fabrication of polydimethylsiloxane (PDMS) microfluidic channels, was purchased from Dow Corning. All chemicals were purchased in standard purities provided by the vendors and used as received. The photoinitiator lithium phenyl-2,4,6-trimethylbenzoylphosphine (LAP) was synthesized according to a previously published procedure.^[64] Reverse osmosis water (MilliQ) was used for all experiments (18.2 M Ω at 25 °C).

Crawler Fabrication: Crawlers were fabricated using stop-flow lithography as previously described.^[20] Briefly: 100 μL of 1–1.5% w/w gold nanoparticles dispersion (diam. = 15 nm, synthesized using citrate method)^[65]

was mixed with NIPAM (37 mg, 327 μmol), PEGDA (20 μL , 29 μmol), and LAP (1.5 mg, 5 μmol). The mixture was sonicated for 5 min to dissolve the components. The pregel solution was always used the same day and centrifuged before use to remove dust and gold colloid agglomerates (2 min at 5000 \times g). To produce hydrogel microcrawlers, the resulting mixture was processed in stop-flow lithography, which was performed as previously described.^[20,66]

After synthesis (typically several thousands of crawlers were prepared in one run), the channel was purged with 0.5% aqueous Tween 20 solution (150 μL) and the crawlers were collected inside the PCR tube. The dispersion containing the crawlers was washed with Tween 20 solution 4 times and allowed to sediment under gravity for 5 min between each washing step. The Tween 20 prevented the crawlers to stick irreversibly to each other and to the container surface.

Experimental Well Fabrication: Surfaces with depression were made by vacuum forming of a 0.5 mm-thick PMMA sheet. The sheet plate 3 by 3 cm was attached to a flat surface with a 4 mm-diameter hole with a source of vacuum in the center. The resulting depression was created by the application of a vacuum and a heat gun for 10 s. Subsequently, a cut-off Eppendorf tube was dipped into PDMS (volume ratio base: curing agent = 10:1), placed onto the prepared surface, and cured overnight at 65 °C.

Optical Setup for Moving/Steering Crawlers: A 200 mW diode laser 532 nm was attenuated using a grey filter (optical density = 0.5) and reflected into the condenser lens of an inverted microscope (Nikon Ti-U) by a short-pass (450 nm) dichroic mirror. The condenser was used to focus the laser beam on the sample plane. The sample well with crawlers was placed under the inverted microscope with the laser setup installed. The laser beam was aimed at a particular part of the crawler and laser pulses (0.5–0.7 s on, 1–1.5 s off) were applied. A 536 nm long-pass filter was placed underneath the sample to block the laser beam from reaching the objective. For automatic disc navigation, a previously developed software was used.^[49]

Parallel Self-Assembly: The wells for parallel self-assembly experiments were prepared by pipetting 35 μL of the Sylgard elastomer base and curing agent mixture (10:1 v:v) into one cylindrical well of a 96-well plate and curing overnight at 65 °C. The bowl shape of the elastomer was produced by the wetting of the well walls by the elastomer. Between 100 and 1000 disc crawlers dispersed in 330 μL of 5% (w/w) Pluronic 127 was pipetted into a well. The sample was left overnight.

Binding: 230 μL of the solution above the self-assembled discs was replaced by 100 μL of water solution of LAP (4% w/w), to reach the final concentration of LAP 2%. In some experiments, PEGDA was added to the binding solution together with the LAP (final PEGDA concentration = 2% w/w). Note, the buckling behavior was identical for the systems with and without added PEGDA (Figure S10, Supporting Information). The solution was left overnight to allow the reagents to diffuse uniformly through the volume. Then the sample was irradiated under the Nikon inverted microscope, using the episcopic illumination from the X-Cite source 220DC (200 W) attenuated to 0.045 of the full intensity. A 4 \times objective and long-pass dichroic mirror 420 nm was used for episcopic illumination and simultaneous diascopic observation. Illumination intensity during the disc binding was estimated (Thorlabs Microscope slide power sensor head for low powers) to be 50 mW cm^{−2}. Specific irradiation patterns were achieved by placing a black-transparent mask to the projection plane, at the position of the EPI illumination field aperture in the microscope. The masks were printed with a standard laser printer on a transparent foil sheet.

Sheet Bulk Heating: The sheet was sedimented in water in a well of 96-well plate. Copper wire (2 mm diam, 1 cm length), attached to a Peltier element, was immersed into the well together with a thermistor and connected to a temperature controller. The well was heated at a rate of ≈ 5 °C min^{−1} from 25 to 80 °C and then allowed to cool down. Three consecutive heating–cooling cycles were applied.

Microscopy: Nikon Eclipse Ti-2 inverted microscope was equipped with 200 W X-Cite mercury lamp source was used for SFL synthesis, widefield fluorescent, and diascopic observation of samples. Acquired diascopic images were processed in the ImageJ software, using the following

protocol: A copy of the image was convolved with a Gaussian filter (with kernel size 20×20 px) and the blurred image was subtracted from the original image to suppress uneven sample illumination. Subsequently, the brightness and contrast of the resulting image were adjusted manually. Confocal microscopy characterization was carried out using Olympus IX81 inverted microscope with FluoView FV1000 confocal system. Labeled microgels were captured by $40\times$ objective (UCPlanFL N, $20\times/0.70$) of the laser scanning confocal microscope using a 488 nm laser for excitation.

Supporting Information

Supporting Information is available from the Wiley Online Library or from the author.

Acknowledgements

This project has received funding from the UCT Institutional Support of 'Marie Prochazkova' fund. I.R. acknowledges his J. E. Purkyne fellowship. The work of C.M. and J.K. was supported by the grant of Specific University Research (grant no. A1_FCHI_2022_006). The work of P.C. was supported by the European Regional Development Fund, OP RDE, Project: CARAT (No. CZ.02.1.01/0.0/0.0/16_026/0008382).

Conflict of Interest

The authors declare no conflict of interest.

Data Availability Statement

The data that support the findings of this study are available from the corresponding author upon reasonable request.

Keywords

hydrogels, microrobots, photothermal, soft actuators

Received: February 21, 2023

Revised: May 5, 2023

Published online:

- [1] X.-Z. Chen, B. Jang, D. Ahmed, C. Hu, C. De Marco, M. Hoop, F. Mushtaq, B. J. Nelson, S. Pané, *Adv. Mater.* **2018**, *30*, 1705061.
- [2] H. Lee, C. Xia, N. X. Fang, *Soft Matter* **2010**, *6*, 4342.
- [3] H. Zeng, P. Wasylczyk, C. Parmeggiani, D. Martella, M. Burrelli, D. S. Wiersma, *Adv. Mater.* **2015**, *27*, 3883.
- [4] M. Rogó, H. Zeng, C. Xuan, D. S. Wiersma, P. Wasylczyk, *Adv. Opt. Mater.* **2016**, *4*, 1689.
- [5] S. Maeda, Y. Hara, T. Sakai, R. Yoshida, S. Hashimoto, *Adv. Mater.* **2007**, *19*, 3480.
- [6] K. Vollmers, D. R. Frutiger, B. E. Kratochvil, B. J. Nelson, *Appl. Phys. Lett.* **2008**, *92*, 144103.
- [7] M. F. Reynolds, A. J. Cortese, Q. Liu, Z. Zheng, W. Wang, S. L. Norris, S. Lee, M. Z. Miskin, A. C. Molnar, I. Cohen, P. L. McEuen, *Sci. Robot.* **2022**, *7*, eabq2296.
- [8] M. Z. Miskin, A. J. Cortese, K. Dorsey, E. P. Esposito, M. F. Reynolds, Q. Liu, M. Cao, D. A. Muller, P. L. McEuen, I. Cohen, *Nature* **2020**, *584*, 557.
- [9] W. Hu, G. Z. Lum, M. Mastrangeli, M. Sitti, *Nature* **2018**, *554*, 81.

- [10] S. Palagi, A. G. Mark, S. Y. Reigh, K. Melde, T. Qiu, H. Zeng, C. Parmeggiani, D. Martella, A. Sanchez-Castillo, N. Kapernaum, F. Giesselmann, D. S. Wiersma, E. Lauga, P. Fischer, *Nat. Mater.* **2016**, *15*, 647.
- [11] O. Aydin, X. Zhang, S. Nuethong, G. J. Pagan-Diaz, R. Bashir, M. Gazzola, M. T. A. Saif, *PNAS* **2019**, *116*, 19841.
- [12] J.-C. Kuo, H.-W. Huang, S.-W. Tung, Y.-J. Yang, *Sens. Actuator. A: Phys.* **2014**, *211*, 121.
- [13] M. Gauthier, E. Gibeau, D. Heriban, in *2006 9th International Conference on Control, Automation, Robotics and Vision*, Singapore **2006**, pp. 1–6, <https://doi.org/10.1109/ICARCV.2006.345273>.
- [14] J. C. Breger, C. Yoon, R. Xiao, H. R. Kwag, M. O. Wang, J. P. Fisher, T. D. Nguyen, D. H. Gracias, *ACS Appl. Mater. Interfaces* **2015**, *7*, 3398.
- [15] H. Zeng, P. Wasylczyk, D. S. Wiersma, A. Priimagi, *Advanced Materials* **2017**, *30*, 1703554.
- [16] M. Sitti, D. S. Wiersma, *Adv. Mater.* **2020**, *32*, 1906766.
- [17] Q. L. Zhu, C. Du, Y. Dai, M. Daab, M. Matejdes, J. Breu, W. Hong, Q. Zheng, Z. L. Wu, *Nat. Commun.* **2020**, *11*, 5166.
- [18] A. Mourran, H. Zhang, R. Vinokur, M. Möller, *Adv. Mater.* **2017**, *29*, n/a.
- [19] H. Zhang, L. Koenen, E. Lauga, A. Mourran, M. Möller, *Small* **2019**, *15*, 1903379.
- [20] I. Rehor, C. Maslen, P. G. Moerman, B. G. P. van Ravensteijn, R. van Alst, J. Groenewold, H. B. Eral, W. K. Kegel, *Soft Robotics* **2020**.
- [21] J. Seo, J. Paik, M. Yim, *Ann. Rev. Control Robot. Auton. Sys.* **2019**, *2*, 63.
- [22] C. Zhang, P. Zhu, Y. Lin, Z. Jiao, J. Zou, *Adv. Intell. Syst.* **2020**, *2*, 1900166.
- [23] A. Spröwitz, R. Moeckel, M. Vespignani, S. Bonardi, A. J. Ijspeert, *Robot. Auton. Sys.* **2014**, *62*, 1016.
- [24] N. B. Crane, O. Onen, J. Carballo, Q. Ni, R. Guldiken, *Microfluid. Nanofluid.* **2013**, *14*, 383.
- [25] X. Yang, R. Tan, H. Lu, T. Fukuda, Y. Shen, *Nat. Commun.* **2022**, *13*, 4156.
- [26] X. Yang, R. Tan, H. Lu, Y. Shen, *IEEE/ASME Trans. Mechatron.* **2022**, *27*, 3590.
- [27] T. M. Schneider, S. Mandre, M. P. Brenner, *Phys. Rev. Lett.* **2011**, *106*, 094503.
- [28] Y. Hoshino, T. Gyobu, K. Imamura, A. Hamasaki, R. Honda, R. Horii, C. Yamashita, Y. Terayama, T. Watanabe, S. Aki, Y. Liu, J. Matsuda, Y. Miura, I. Taniguchi, *ACS Appl. Mater. Interfaces* **2021**, *13*, 30030.
- [29] H. Wang, J. Li, J. Cui, Q. Shi, Z. Zheng, T. Sun, Q. Huang, T. Fukuda, *IEEE Trans. Nanotechnol.* **2018**, *17*, 684.
- [30] J. Zemánek, T. Michálek, Z. Hurák, *Lab Chip* **2018**, *18*, 1793.
- [31] L. Cademartiri, K. J. M. Bishop, P. W. Snyder, G. A. Ozin, *Philos. Trans. Royal Soc. A: Math. Phys. Eng. Sci.* **2012**, *370*, 2824.
- [32] M. Mastrangeli, in *2017 19th Inter. Conf. on Solid-State Sensors, Actuators and Microsystems (TRANSDUCERS)*, Kaohsiung, Taiwan **2017**, pp. 676–681, <https://doi.org/10.1109/TRANSDUCERS.2017.7994139>.
- [33] M. Mastrangeli, G. Mermoud, A. Martinoli, *Micromachines* **2011**, *2*, 82.
- [34] G. Gardi, S. Ceron, W. Wang, K. Petersen, M. Sitti, *Nat. Commun.* **2022**, *13*, 2239.
- [35] D. J. Kraft, J. Hilhorst, M. A. P. Heinen, M. J. Hoogenraad, B. Luijckes, W. K. Kegel, *J. Phys. Chem. B* **2011**, *115*, 7175.
- [36] P. Tierno, *Phys. Chem. Chem. Phys.* **2014**, *16*, 23515.
- [37] H. Wei, Y. Chen, J. Tan, T. Wang, *IEEE/ASME Trans. Mechatron.* **2011**, *16*, 745.
- [38] H. Oh, A. Ramezan Shirazi, C. Sun, Y. Jin, *Rob. Auton. Syst.* **2017**, *91*, 83.
- [39] N. Bredeche, E. Haasdijk, A. Prieto, *Front. Robot. AI* **2018**, *5*, <https://doi.org/10.3389/frobt.2018.00012>.
- [40] S. Garnier, C. Jost, J. Gautrais, M. Asadpour, G. Caprari, R. Jeanson, A. Grimal, G. Theraulaz, *Artif. Life* **2008**, *14*, 387.
- [41] S. Griffith, D. Goldwater, J. M. Jacobson, *Nature* **2005**, *437*, 636.

- [42] B. R. Donald, C. G. Levey, I. Paprotny, *J. Microelectromech. Syst.* **2008**, 17, 789.
- [43] G. M. Whitesides, M. Boncheva, *Proc. Natl. Acad. Sci.* **2002**, 99, 4769.
- [44] M. H. Lash, M. V. Fedorchak, S. R. Little, J. J. McCarthy, *Langmuir* **2015**, 31, 898.
- [45] M. Mastrangeli, Q. Zhou, V. Sariola, P. Lambert, *Soft Matter* **2017**, 13, 304.
- [46] S. Guven, P. Chen, F. Inci, S. Tasoglu, B. Erkmen, U. Demirci, *Trends Biotechnol* **2015**, 33, 269.
- [47] B. Zamanian, M. Masaeli, J. W. Nichol, M. Khabiry, M. J. Hancock, H. Bae, A. Khademhosseini, *Small* **2010**, 6, 937.
- [48] Y. N. Vakkipurath Kodakkadan, C. Maslen, P. Cigler, F. Štěpánek, I. Rehor, *J. Mater. Chem. B* **2021**, 9, 4718.
- [49] J. Vrba, C. Maslen, J. Maxova, J. Duras, I. Rehor, J. Mares, *J. Comput. Sci.* **2021**, 55, 101446.
- [50] B. M. Jose, T. Cubaud, *Microfluid Nanofluid* **2012**, 12, 687.
- [51] J. G. Fernandez, A. Khademhosseini, *Adv. Mater.* **2010**, 22, 2538.
- [52] T. Canal, N. A. Peppas, *J. Biomed. Mater. Res.* **1989**, 23, 1183.
- [53] G. Stoychev, S. Zakharchenko, S. Turcaud, J. W. C. Dunlop, L. Ionov, *ACS Nano* **2012**, 6, 3925.
- [54] V. Luchnikov, O. Sydorenko, M. Stamm, *Adv. Mater.* **2005**, 17, 1177.
- [55] I. S. Chun, A. Challa, B. Derickson, K. J. Hsia, X. Li, *Nano Lett.* **2010**, 10, 3927.
- [56] M. Pezzulla, G. P. Smith, P. Nardinocchi, D. P. Holmes, *Soft Matter* **2016**, 12, 4435.
- [57] G. G. Odian, in *Principles of Polymerization*, Wiley-Interscience, Hoboken, NJ **2004**.
- [58] S.-J. Jeon, A. W. Hauser, R. C. Hayward, *Acc. Chem. Res.* **2017**, 50, 161.
- [59] R. Luo, J. Wu, N.-D. Dinh, C.-H. Chen, *Adv. Funct. Mater.* **2015**, 25, 7272.
- [60] W. Fan, C. Shan, H. Guo, J. Sang, R. Wang, R. Zheng, K. Sui, Z. Nie, *Science Advances* **2019**, 5, eaav7174.
- [61] A. Cangialosi, C. Yoon, J. Liu, Q. Huang, J. Guo, T. D. Nguyen, D. H. Gracias, R. Schulman, *Science* **2017**, 357, 1126.
- [62] R. F. Shepherd, F. Ilievski, W. Choi, S. A. Morin, A. A. Stokes, A. D. Mazzeo, X. Chen, M. Wang, G. M. Whitesides, *Proc. Natl. Acad. Sci. U S A* **2011**, 108, 20400.
- [63] W. Wang, J.-Y. Lee, H. Rodrigue, S.-H. Song, W.-S. Chu, S.-H. Ahn, *Bioinspir. Biomim.* **2014**, 9, 046006.
- [64] B. D. Fairbanks, M. P. Schwartz, C. N. Bowman, K. S. Anseth, *Biomaterials* **2009**, 30, 6702.
- [65] G. Frens, *Nat. Phy. Sci.* **1973**, 241, 20.
- [66] D. Dendukuri, S. S. Gu, D. C. Pregibon, T. Alan Hatton, P. S. Doyle, *Lab Chip* **2007**, 7, 818.